Supplementary information for

Combining energy and electron transfer in a supramolecular environment for the "green" generation and utilization of hydrated electrons through photoredox catalysis

*By Christoph Kerzig and Martin Goez**

Contents

1 General experimental details

For the laser flash photolysis measurements, a two-pulse nanosecond system with optical detection was employed. A detailed description of our setup has been given previously.[S1] Briefly, the individually collimated beams of two frequency-doubled Nd:YAG lasers (532 nm) were used to irradiate the solutions, which were pumped through a suprasil cell. Transient absorptions and emissions were monitored at right angle to the excitation beam. A uniform concentration of transient species in the cell was ensured by keeping the substance concentrations so low that less

than 4 % of the laser light was absorbed. For supporting experiments that required UV excitation, a frequency-tripled Nd:YAG laser (355 nm) or a XeCl excimer laser (308 nm) was used.

All commercially available chemicals were obtained in the highest purity and used as received (pyrene-1-carboxylic acid, 97 %, Aldrich; pyrene-1-butyric acid, >98 %, TCI; ruthenium-tris(bipyridine) dichloride hexahydrate, 99 %, abcr; ruthenium-tris(phenanthroline) dichloride hydrate, 98 %, Aldrich; ruthenium-tris(4,7-diphenyl-1,10-phenanthroline) dichloride, Alfa Aesar; sodium ascorbate, ≥ 99 %, Roth; sodium dodecyl sulfate, ≥ 99.5 %, Roth; sodium chloroacetate, 98 %, Aldrich; 4-methoxy phenol, 99 %, Aldrich; sodium hydroxide for adjusting the pH, >99 %, Aldrich). Ultrapure Millipor MilliQ water (specific resistance, 18.2 MΩ cm) was the solvent throughout.

To avoid degradation, all solutions were freshly prepared in the dark, and then immediately purged with argon (5.0, Air Liquide) or N_2O (5.0, Air Liquide) for 30 minutes before and for the whole duration of the laser flash photolysis experiments. To prevent the oxidation of ascorbate by molecular oxygen,[S2] which is quite fast in alkaline aqueous solution, the required amount of sodium ascorbate was added in solid form to the already degassed solutions.

Steady-state absorption and luminescence spectra were measured using a UV-2102 spectrophotometer (Shimadzu) and a LS 50B spectrometer (Perkin Elmer), respectively.

2 Quantum mechanical computations

Quantum mechanical computations of the ground state $\mathbf{Py}^-$, triplet state $^3\mathbf{Py}^-$, and radical anion $\mathbf{Py}^{\bullet 2-}$ of the redox catalyst were carried out with the Gaussian 09 package[S3]. Since Hartree–Fock calculations with the basis set 6-31G(d,p) have already proven successful for explaining experimental observations on $\mathbf{Py}^-$,[S4] these methods were used for our initial calculations as well. Our results for the optimized structure and the dipole moment of $\mathbf{Py}^-$ perfectly agree with those reported by Nucci *et al.*[S4]. To visualize the effect of the carboxylate substituent on the pyrene chromophore, we computed the orbitals of $\mathbf{Py}^-$ by an NBO population analysis. As is seen from the orbitals presented in Figure S1, the carboxylate substituent neither affects the π orbitals of the ring significantly (HOMO, LUMO) nor is its negative charge considerably delocalized over the pyrene skeleton (HOMO-2). Moreover, as we found, the frontier orbitals as well as the other ring π orbitals of $\mathbf{Py}^-$ are virtually identical to those of unsubstituted pyrene.

The optimized structure of $\mathbf{Py}^-$, together with the dipole vector and the NBO charges, is displayed in Figure S2 (left). Despite the agreement of the $\mathbf{Py}^-$ structure and dipole moment with the previous calculations[S4], the NBO charges differ substantially. We have no explanation for the discrepancies but note that the charges in Ref.[S4] incorrectly sum to zero, whereas the total of our charges equals the expected value for the monoanion, -1.

To avoid HF optimizations with computationally intensive configuration interactions, which would be necessary to describe the pyrene species with singly occupied orbitals, *i.e.*, $^3\mathbf{Py}^-$ and

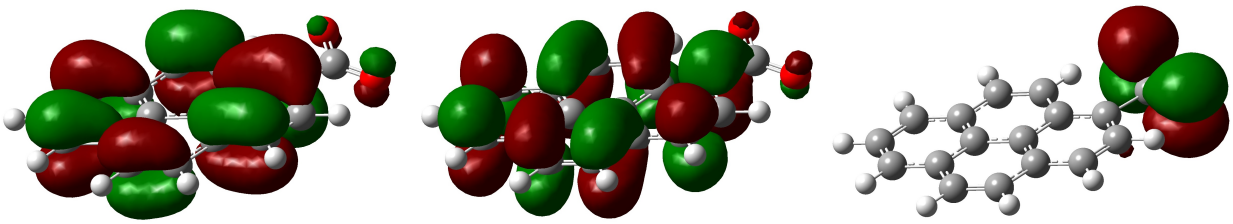

Figure S1: Representative orbitals of $\mathbf{Py}^-$ (left, HOMO; center, LUMO; right, HOMO−2) computed at the HF/6-31G(d,p) level of theory. Further explanation, see text.

$\mathbf{Py}^{\bullet 2-}$, we used DFT calculations with the B3LYP functional because this method is known to be well-suited for the efficient computation of complex molecules or even open-shell species[S5–S7]. Furthermore, as a refinement over Ref.[S4] we added diffuse functions on heavy atoms as they are recommended for calculations on anionic species[S8]. Before turning to $^3\mathbf{Py}^-$ and $\mathbf{Py}^{\bullet 2-}$, we compared the HF and DFT calculations of $\mathbf{Py}^-$. As is evident from Figure S2 and Table S1, the results provided by these methods — including geometry, dipole moment and charge distribution — are very similar.

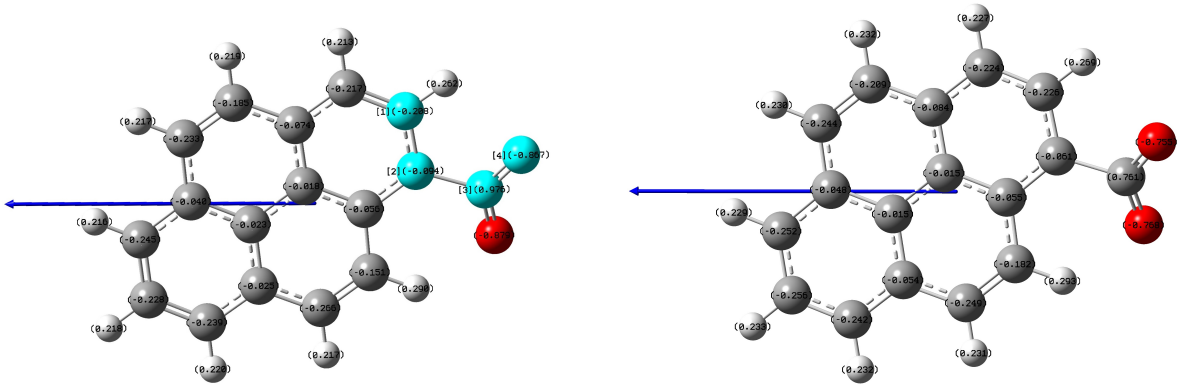

Figure S2: Comparison of the optimized structures, charge distributions and dipole orientations of $\mathbf{Py}^-$ obtained with HF/6-31G(d,p) (left) and B3LYP/6-31+G(d,p) (right). The blue atoms in the left structure span the dihedral angle of Table S1. For details, see text.

For $^3\mathbf{Py}^-$, compared to $\mathbf{Py}^-$, we obtained a more twisted structure, a slightly shorter length of the C–C bond between ring and substituent and a dipole moment decrease by less than 20 % (see, Figure S3 and Table S1). This is due to a weak charge migration from carboxylate to pyrene upon conversion of $\mathbf{Py}^-$ into $^3\mathbf{Py}^-$ (compare, the charge distributions presented in Figures S2 (right) and S3). The shortened C–C distance is still comparable to an aliphatic bond indicating the negligible influence of the carboxylate compared to the protonated substituent, COOH, which causes a significant contraction of the respective C–C bond and clearly influences the pyrene chromophore[S4].

Because of the delocalization of the further negative charge mainly over the pyrene ring system, the dipole moment of the radical anion $\mathbf{Py}^{\bullet 2-}$ is about two-thirds lower than that of $\mathbf{Py}^-$ (Table S1).

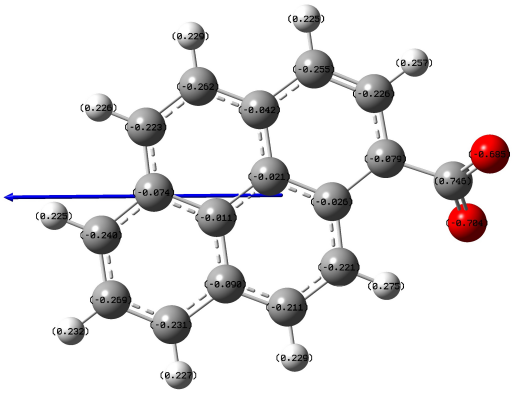

Figure S3: Optimized structure, charge distribution and dipole orientation of $^3\mathbf{Py}^-$ (B3LYP/6-31+G(d,p)).

species	dipole moment	dihedral angle[c]	C–C bond length[d]
$\mathbf{Py}^-$[a]	13.8 D	16.3°	1.56 Å
$\mathbf{Py}^-$[b]	14.2 D	27.5°	1.56 Å
$^3\mathbf{Py}^-$[b]	11.8 D	45.8°	1.51 Å
$\mathbf{Py}^{\bullet 2-}$[b]	5.3 D	3.0°	1.56 Å

[a] HF/6-31G(d,p). [b] B3LYP/6-31+G(d,p). [c] Dihedral angle as highlighted in Figure S2 (left). [d] C–C bond between ring and substituent.

Table S1: Computed dipole moments, dihedral angles and bond lengths of the pyrene species in our system. For details, see text.

All geometry optimizations were accompanied by frequency analyses, which did not yield negative vibrational frequencies, indicating convergence on minimum energy structures.

3 Absorption spectra and pertinent properties of all species

Figure S4 displays the calibrated UV-Vis absorption spectra of all chemical species in our system. Further information concerning the spectral calibration of exited states or radical ions is given in the sections below.

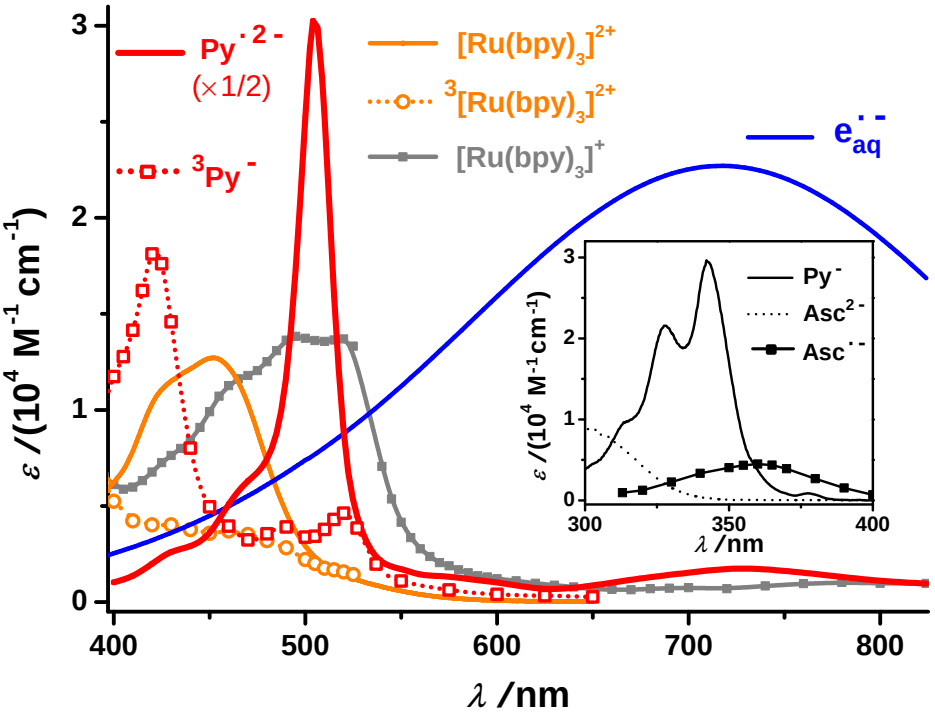

Figure S4: Calibrated absorption spectra (in aqueous solution at pH 12.7 containing 30 mM SDS) of all species in our system. For clarity, the spectral range has been divided into two parts, 300 – 400 nm (inset) and 400 – 825 nm (main plot); moreover, the spectrum of $\mathbf{Py}^{\bullet 2-}$ has been multiplied by 1/2. For abbreviations and further details, see text.

3.1 Ground state Py^- of pyrene-1-carboxylate

The pK_a value of pyrene-1-carboxylic acid is 4,[S9,S10] hence, the carboxylate ($\mathbf{Py}^-$) is its only form existing under our experimental conditions (pH 12.7). Although $\mathbf{Py}^-$ is a strong photobase with a pK_a increase by up to 4 units in the lowest excited states,[S10] a protonation of excited $\mathbf{Py}^-$ does not occur in our strongly alkaline reaction medium.

$\mathbf{Py}^-$ absorbs light below 390 nm (see, Figure S4) with a spectrum that is quite similar to that of pyrene in polar solvents[S11].

When sodium dodecyl sulfate (SDS) is added at concentrations above the critical micelle concentration (cmc), the absorption spectrum of $\mathbf{Py}^-$ exhibits a slight red shift and a decrease in molar absorptivity (Figure S5, main plot), indicating a compartmentalization of $\mathbf{Py}^-$ in the anionic micelles.

To determine the association constant of $\mathbf{Py}^-$ with the SDS micelles, we recorded its absorption spectrum at various SDS concentrations, and performed a Benesi–Hildebrand[S12] analysis for the wavelengths with the most pronounced absorption changes, 340 and 351 nm (Figure S5, inset). The concentrations of SDS micelles were calculated from the starting surfactant concentrations with the average aggregation number (60)[S13] and the cmc (8.2 mM)[S13]. The linear Benesi–Hildebrand plots at both detection wavelengths clearly identify the association as a 1:1 process; the parameters of the linear regressions yield very similar association constants with an average value of 700 M^{-1}. With that constant, the fraction of $\mathbf{Py}^-$ that is bound to the micelles can be calculated. It amounts to 0.2 under the general conditions of this study (30 mM SDS; compare, main paper). We also investigated the association of pyrene-1-butyrate with SDS micelles using the same experimental method as displayed in Figure S5 and obtained an association constant of 25000 M^{-1}, which is in good agreement with the result of a previous study (24000 M^{-1})[S14].

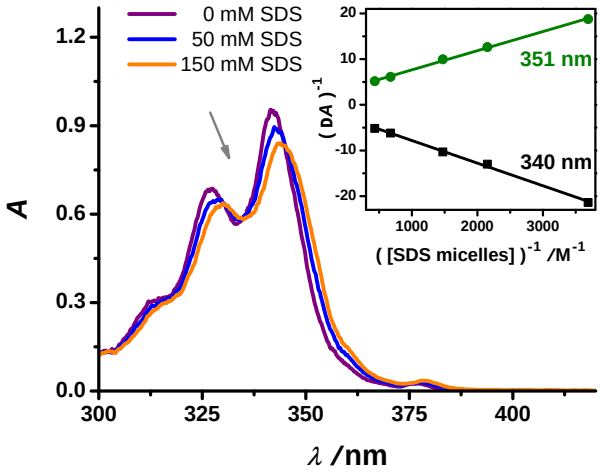

Figure S5: Main plot, changes of the absorption spectrum of an aqueous solution of $\mathbf{Py}^-$ (3×10^{-5} M) at pH 12.7 upon the addition of SDS. Inset, Benesi–Hildebrand plot of the absorbance changes at 340 and 351 nm. For further details, see text.

For supporting experiments with generation of $^3\mathbf{Py}^-$ or $\mathbf{Py}^{\bullet 2-}$ in the absence of $[\mathbf{Ru(bpy)_3}]^{2+}$ (see, Sections 3.2 and 3.3), we directly excited $\mathbf{Py}^-$ with a 355 nm laser pulse that was sufficiently attenuated to suppress a biphotonic ionization, which otherwise is a typical photoreaction of water-soluble pyrene derivatives[S15,S16].

For the triplet energy and reduction potential of $\mathbf{Py}^-$, which enter Figure 1b of the main paper, we have taken the values of pyrene in polar solvents[S11] because the absorption spectra of

the carboxylate and its unsubstituted parent are extremely similar in all relevant forms (ground state, triplet, and radical anion) and the differences of the Hammett constants for COO^- and H are negligible.[S11]

3.2 Triplet state $^3Py^-$

To investigate the triplet-triplet energy transfer from the green-light excited $^3[\mathbf{Ru(bpy)_3}]^{2+}$ to $\mathbf{Py}^-$ (reaction EnT), we used the $^3[\mathbf{Ru(bpy)_3}]^{2+}$ luminescence (emission maximum, 620nm), which exclusively responds to the concentration of the energy donor, without any interference from other species in our system.

In homogeneous aqueous solution (Figure S6a, main plot), all luminescence traces decay with clear first-order kinetics (fit function, $I(t) = I(0) \times \exp[-t/\tau]$). With increasing $\mathbf{Py}^-$ concentration, the amplitude $I(0)$ remains constant whereas the lifetime τ decreases, indicating purely dynamic quenching. The Stern–Volmer plots (Figure S6a, inset) are linear regardless of whether they are based on the luminescence lifetimes τ_0/τ or on the integrated luminescence curves I_0/I, and yield a rate constant of $5.4 \times 10^9\,M^{-1}\,s^{-1}$.

In aqueous micellar solution of SDS, the mechanism of the triplet-triplet energy transfer is more complex (Figure S6b). There is only a negligible contribution of static quenching (less than 5 % under our experimental conditions), but the luminescence decay becomes biphasic and the Stern–Volmer plot exhibits a slight downward curvature, which is typical for a reduced accessibility of some fraction of the strongly micelle-bound luminophore to the quencher largely residing in the aqueous phase.[S17]

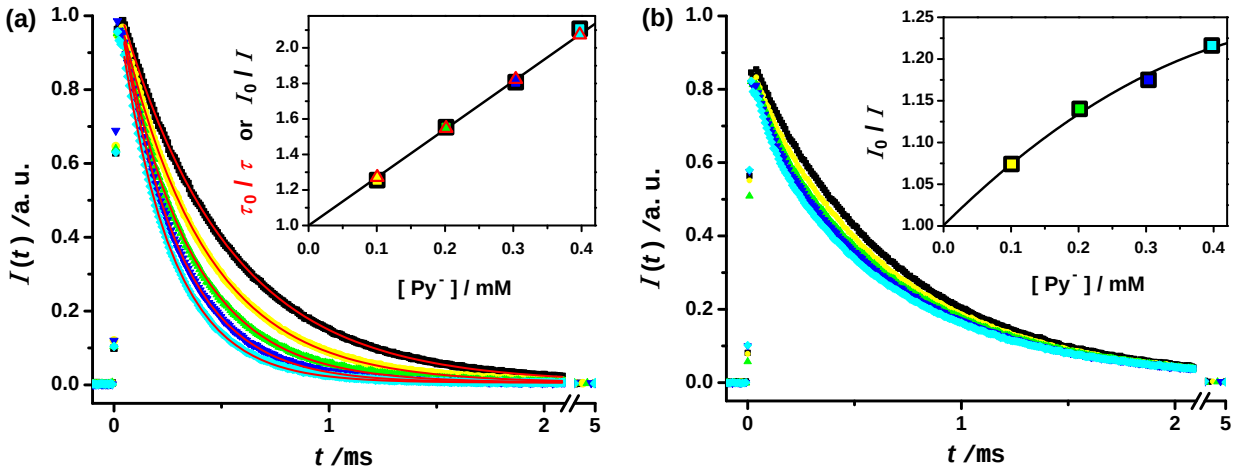

Figure S6: Energy transfer from $^3[\mathbf{Ru(bpy)_3}]^{2+}$ to $\mathbf{Py}^-$ studied by time-resolved measurements of the $^3[\mathbf{Ru(bpy)_3}]^{2+}$ luminescence at 620 nm, $I(t)$, in deoxygenated aqueous solutions of 6×10^{-5} M $[\mathbf{Ru(bpy)_3}]^{2+}$ at pH 12.7, upon excitation with a 532 nm pulse of 351 mJ cm^{-2}; (a), without SDS; (b), with 30 mM SDS. Each main plot shows the luminescence traces at different $\mathbf{Py}^-$ concentrations (black, 0 mM; yellow, 0.1 mM; green, 0.2 mM; blue, 0.3 mM; light blue, 0.4 mM). The insets give the corresponding Stern–Volmer plots on the basis of the integrated luminescence curves I_0/I (squares), and in (a) additionally on that of the lifetimes τ_0/τ (triangles), using the same colour coding for the concentrations as in the main plots. For further details, see text.

Under the experimental conditions of the main paper (6×10^{-5} M $[\mathbf{Ru(bpy)_3}]^{2+}$ and 3×10^{-4} M $\mathbf{Py}^-$) the energy transfer efficiencies, calculated from $1 - I/I_0$, are 0.45 in homogeneous aqueous solution and 0.15 in 30 mM SDS micellar solution. Neglecting the small curvature of the Stern–Volmer plot, the latter efficiency corresponds to an apparent rate constant of $8.8 \times 10^8\,\mathrm{M^{-1}\,s^{-1}}$ for the energy transfer in SDS. A higher SDS concentration does not appreciably increase the transfer efficiency because the static contribution is too small, and a lower SDS concentration is detrimental because it increases the number of micelles occupied by two $[\mathbf{Ru(bpy)_3}]^{2+}$ molecules, which results in fast self-quenching of $^3[\mathbf{Ru(bpy)_3}]^{2+}$.[S18]

The small energy difference of only 0.03 eV between $^3[\mathbf{Ru(bpy)_3}]^{2+}$ and $^3\mathbf{Py}^-$[S11] implies a reversibility of the energy transfer. Although we could not detect a delayed luminescence of $^3[\mathbf{Ru(bpy)_3}]^{2+}$, we observed shorter lifetimes of $^3\mathbf{Py}^-$ in the presence of the light-harvesting complex (10 µs in water and 16 µs in 30 mM aqueous SDS) compared to experiments in its absence (25 µs in both media), for which we accessed $^3\mathbf{Py}^-$ by exciting $\mathbf{Py}^-$ with a 355 nm pulse followed by fast intersystem crossing[S9]. A closed-form solution of the kinetic equations in homogeneous solution was obtained by Mathematica® and yielded a biexponential time-dependence. From the slower of the two apparent rate constants, which dominates the long-time behaviour, we extracted a rate constant of $1.8 \times 10^9\,\mathrm{M^{-1}\,s^{-1}}$ for the energy transfer from $^3\mathbf{Py}^-$ to ground-state $[\mathbf{Ru(bpy)_3}]^{2+}$; the experimental equilibrium constant is thus in perfect agreement with the one calculated from the reported[S11] triplet energies. We stress that the reverse energy transfer is rendered negligible under the experimental conditions of the main paper, where $^3\mathbf{Py}^-$ is rapidly removed by the sacrificial donor $\mathbf{Asc}^{2-}$ (see, Section 3.3).

The absorption spectra of $^3\mathbf{Py}^-$ obtained under the conditions of Figure S6 are virtually identical in water and in 30 mM SDS, except for a scaling factor reflecting the different degrees of energy transfer. They show maxima at 420 nm and 520 nm, which are in good agreement with those of pyrene in polar solvents[S11] and those of other pyrene derivatives in aqueous solution[S15]. The absolute extinction coefficient was calibrated with the known extinction coefficient of $^3[\mathbf{Ru(bpy)_3}]^{2+}$ as the reference[S1] and the energy transfer efficiency determined as described above.

In control experiments on $^3\mathbf{Py}^-$ alone, *i.e.*, generated with a 355 nm pulse in the absence of light-harvesting complex and sacrificial donor, we did not observe any bleaching or electron formation upon excitation with an intense green laser pulse. Hence, despite an absorption band in that range (compare, Figure S4), the triplet $^3\mathbf{Py}^-$ is photostable at 532 nm.

3.3 Radical anion $\mathbf{Py}^{\bullet 2-}$

To isolate the reactions involving $\mathbf{Py}^{\bullet 2-}$ but not the light-harvesting complex, we produced $^3\mathbf{Py}^-$ with 355 nm as described above, and quenched it with the sacrificial donor $\mathbf{Asc}^{2-}$. Figure S7a displays experimental absorption traces recorded at 504 nm, the maximum of the $\mathbf{Py}^{\bullet 2-}$ spectrum, where $^3\mathbf{Py}^-$ contributes negligibly and all ascorbate-derived species are completely transparent

(compare, Figure S4). The time dependences are describable by a formation with the same rate as the $^3\mathbf{Py}^-$ decay, which can be observed at 420 nm, and a subsequent slow decrease of $\mathbf{Py}^{\bullet 2-}$. Whereas the formation rate constant (reaction ET) is about twice as high in homogeneous aqueous solution ($4.9 \times 10^8\,M^{-1}\,s^{-1}$) compared to 30 mM SDS solution ($2.5 \times 10^8\,M^{-1}\,s^{-1}$), the decay of $\mathbf{Py}^{\bullet 2-}$ is largely independent of the environment, suggesting that $\mathbf{Py}^{\bullet 2-}$ does not interact with the anionic micelles. Moreover, the $\mathbf{Py}^{\bullet 2-}$ natural lifetime (67 µs) does not change with the laser power, so does not depend on the concentrations of $\mathbf{Py}^{\bullet 2-}$ or $\mathbf{Asc}^{\bullet -}$. Hence, we conclude that the decay is mainly due to the protonation of $\mathbf{Py}^{\bullet 2-}$ by the solvent to give a product that weakly absorbs at the blue edge of the visible spectrum and is fully transparent above 450 nm; this was also reported in pulse radiolysis studies[S19,S20].

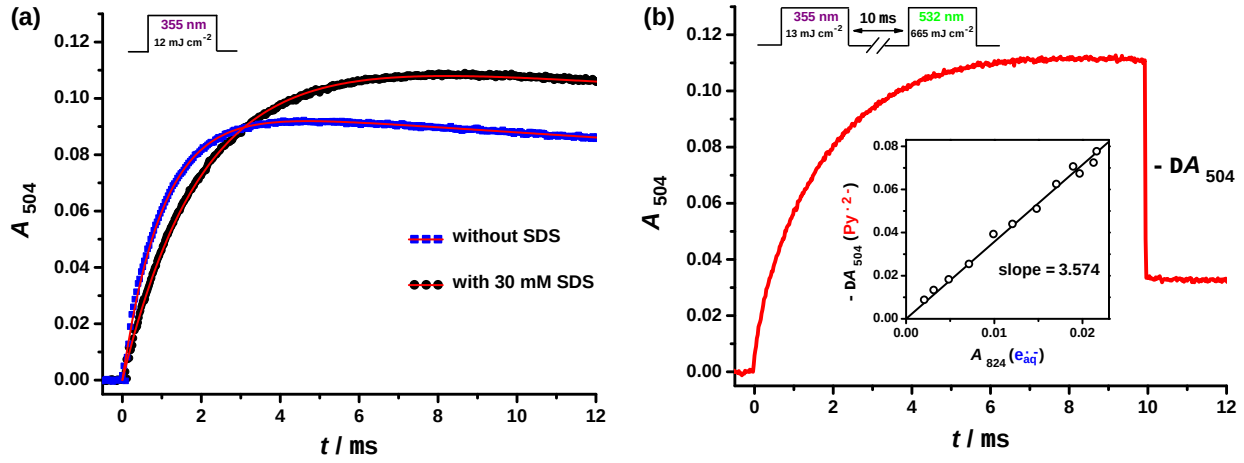

Figure S7: $\mathbf{Py}^{\bullet 2-}$ generation and decay (a) and green-light ionization (b) in the absence of the light-harvesting complex. Pulse schemes given above the traces, deoxygenated aqueous solutions at pH 12.7 of 4×10^{-5} M $\mathbf{Py}^-$ and 2 mM $\mathbf{Asc}^{2-}$. (a) Influence of SDS on the $\mathbf{Py}^{\bullet 2-}$ kinetics. Blue squares (water) and black circles (30 mM SDS), experimental data points for $\mathbf{Py}^{\bullet 2-}$ observed at 504 nm; red solid lines, fits of $R(t) = \frac{k_{ET}}{k_{ET}-k_P}(\exp[-k_P t] - \exp[-k_{ET} t])$ to the $\mathbf{Py}^{\bullet 2-}$ curves with k_P fixed at $1.5 \times 10^4\,s^{-1}$ and the best-fit parameters $k_{ET} = 9.8 \times 10^5\,s^{-1}$ (water) or $k_{ET} = 5.0 \times 10^5\,s^{-1}$ (30 mM SDS). The increased signal height of $\mathbf{Py}^{\bullet 2-}$ in the SDS solution is due to the more efficient excitation caused by a spectral shift (compare, Figure S5) (b) Main plot, $\mathbf{Py}^{\bullet 2-}$ absorption during a two-pulse laser flash photolysis experiment on a solution containing 30 mM SDS and saturated with N_2O. Inset, $\mathbf{Py}^{\bullet 2-}$ bleaching, $-\Delta A_{504}(\mathbf{Py}^{\bullet 2-})$, as a function of the $\mathbf{e}^{\bullet -}_{\mathbf{aq}}$ absorption build-up, $A_{824}(\mathbf{e}^{\bullet -}_{\mathbf{aq}})$, at different intensities of the second laser pulse; other experimental parameters as in the main plot. The slope of the regression line equals the ratio of the molar absorption coefficients of the two species at the respective wavelengths. The separation of $\mathbf{Py}^{\bullet 2-}$ and $\mathbf{e}^{\bullet -}_{\mathbf{aq}}$ signals was carried out as described in Section 3.6. Further explanation, see text.

Because the light-harvesting complex was omitted, the only species absorbing at 532 nm are thus $\mathbf{Py}^{\bullet 2-}$ and $^3\mathbf{Py}^-$, and the latter is photochemically inert at this wavelength. As can be seen in the main plot of Figure S7b, the green pulse bleaches $\mathbf{Py}^{\bullet 2-}$. That bleaching is accompanied by the formation of hydrated electrons $\mathbf{e}^{\bullet -}_{\mathbf{aq}}$ (not shown).

A plot of $\mathbf{Py}^{\bullet 2-}$ bleaching as a function of $\mathbf{e}^{\bullet -}_{\mathbf{aq}}$ formation, which was obtained by varying the intensity of the green laser pulse with all other experimental parameters being identical,

(Figure S7b, inset; for the details of the $\mathbf{e}_{aq}^{\bullet-}$ measurements, see Section 3.6) yields a straight line. That relationship clearly identifies the photoionization of $\mathbf{Py}^{\bullet 2-}$ as the common cause of both effects. The slope of the regression line, together with the molar absorption coefficient of $\mathbf{e}_{aq}^{\bullet-}$ at 824 nm ($\varepsilon_{824}(\mathbf{e}_{aq}^{\bullet-})$=16900 $M^{-1}\,cm^{-1}$), gives a molar absorption coefficient $\varepsilon_{504}(\mathbf{Py}^{\bullet 2-})$ of 60400 $M^{-1}\,cm^{-1}$, provided that every bleached radical anion yields a hydrated electron. But any side reaction would lead to an overestimation of $\varepsilon_{504}(\mathbf{Py}^{\bullet 2-})$, and our value is about 5 % lower than that determined by pulse radiolysis (63800 $M^{-1}\,cm^{-1}$, after recalculation to take into account the currently accepted molar absorption coefficient of $\mathbf{e}_{aq}^{\bullet-}$)[S20,S21], so we conclude that photoionization is the only chemical decay pathway of the excited radical anion. This is in accordance with the absence of side reactions in our recent study on a photoexcited naphthalene radical anion.[S22]

As exemplified by the trace displayed in Figure S7b, a complete two-pulse kinetic spectrum was recorded and the absorption spectrum of $\mathbf{Py}^{\bullet 2-}$ was extracted from the bleaching. Both that absorption spectrum and the intensity dependence of the green-light ionization of $\mathbf{Py}^{\bullet 2-}$ are completely identical in aqueous solution and in SDS (30 mM). All these findings demonstrate that $\mathbf{Py}^{\bullet 2-}$ does not interact with the SDS micelles.

3.4 Ascorbate-derived species

The pK_a of the equilibrium between the ascorbate mono- and dianion, $\mathbf{HAsc}^- \rightleftharpoons \mathbf{Asc}^{2-} + \mathbf{H}^+$, is 11.79.[S2] At the general pH of our experiments, 12.7, $\mathbf{Asc}^{2-}$ is thus the predominant species (89 %). To test whether the small amount of $\mathbf{HAsc}^-$ has any effect, we carried out control experiments as in Figure S7a, but at pH 8. Under these conditions, we did not observe any quenching of $^3\mathbf{Py}^-$; hence, the more reactive[S23] $\mathbf{Asc}^{2-}$ is required for reaction ET (Table 1 of the main paper). The ascorbate radical anion $\mathbf{Asc}^{\bullet-}$ formed in that reaction does not absorb above 450 nm and thus need not be considered in the spectral separation shown in Figure 2b of the main paper. For the calibrated spectrum of $\mathbf{Asc}^{\bullet-}$ in SDS (Figure S4), we generated that radical independently by ionizing $\mathbf{Asc}^{2-}$ (4×10^{-5} M $\mathbf{Asc}^{2-}$, 30 mM SDS) with an intense 308 nm laser pulse and equated the amounts of $\mathbf{Asc}^{\bullet-}$ and $\mathbf{e}_{aq}^{\bullet-}$. The spectrum in SDS is practically identical with that recently obtained by the same procedure in homogeneous aqueous solution[S24]. Although the stability of $\mathbf{Asc}^{\bullet-}$ decreases in strongly alkaline solution,[S25] it still persists for several tens of microseconds under our conditions. In our complete reaction system, we observed no appreciable recombination of $\mathbf{Asc}^{\bullet-}$ and $\mathbf{Py}^{\bullet 2-}$.

3.5 $[\mathbf{Ru(bpy)_3}]^{2+}$ and derived species

We recorded the absorption spectra of the $[\mathbf{Ru(bpy)_3}]^{2+}$-derived intermediates ($^3[\mathbf{Ru(bpy)_3}]^{2+}$ and $[\mathbf{Ru(bpy)_3}]^{+}$) using our laser flash photolysis setup with a single green (532 nm) laser. For their calibration in our reaction medium, aqueous SDS, we applied the same methods as in our

recent investigation[S1]. Briefly, in the case of $^3[\mathbf{Ru(bpy)_3}]^{2+}$, we extrapolated the intensity dependence (compare, the reference curve in the inset of Figure 3a of the main paper) to full conversion of $[\mathbf{Ru(bpy)_3}]^{2+}$ into $^3[\mathbf{Ru(bpy)_3}]^{2+}$; and in the case of $[\mathbf{Ru(bpy)_3}]^{+}$, we quenched the excited state with 4-methoxy phenolate and used the known extinction coefficient of the phenoxy radical, which is formed in the same amount as is $[\mathbf{Ru(bpy)_3}]^{+}$, for comparison. The calibrated spectra in SDS micellar solution (Figure S4), which are corrected for $[\mathbf{Ru(bpy)_3}]^{2+}$ depletion, have very similar shapes compared to aqueous solution[S1] but are slightly red-shifted. Moreover, they do not change when the SDS amount is further increased, indicating that all $[\mathbf{Ru(bpy)_3}]^{2+}$-derived species are quantitatively complexed by the micelles under our general experimental conditions (30 mM SDS). The micellar environment also increases the lifetime of $^3[\mathbf{Ru(bpy)_3}]^{2+}$ somewhat, from 500 ns to 670 ns.

We studied the electron transfer from $\mathbf{Py^{\bullet 2-}}$ to $[\mathbf{Ru(bpy)_3}]^{2+}$ (reaction R) at the isosbestic point of $[\mathbf{Ru(bpy)_3}]^{2+}$ and $[\mathbf{Ru(bpy)_3}]^{+}$, 461 nm (homogeneous aqueous solution) or 464 nm (SDS solution), where the interconversion of the complex-derived species is masked but $\mathbf{Py^{\bullet 2-}}$ absorbs strongly ($\varepsilon(\mathbf{Py^{\bullet 2-}})\approx 10000\,M^{-1}\,cm^{-1}$). From the resulting pseudo first-order rate constants of the $\mathbf{Py^{\bullet 2-}}$ decay in the presence of $[\mathbf{Ru(bpy)_3}]^{2+}$ and the natural life of the aryl radical anion (67 µs; see, Section 3.3), we determined the rate constants of reaction R in micellar ($1.8\times10^7\,M^{-1}\,s^{-1}$) as well as homogeneous aqueous ($6.4\times10^9\,M^{-1}\,s^{-1}$) solution. For the latter measurements, we had to attenuate the laser intensity to minimize the formation of $[\mathbf{Ru(bpy)_3}]^{+}$ through reaction Q, which otherwise is quite efficient in the non-micellar medium.

To separate the transient absorptions of $\mathbf{Py^{\bullet 2-}}$ and $[\mathbf{Ru(bpy)_3}]^{+}$ as displayed in the inset of Figure 2b of the main paper, we again used the pure $\mathbf{Py^{\bullet 2-}}$ signal at the above-mentioned isosbestic point. Normalizing the independently calibrated $\mathbf{Py^{\bullet 2-}}$ spectrum (Section 3.3) to the value at that wavelength yields the contribution of $\mathbf{Py^{\bullet 2-}}$, and subtraction of that contribution gives the difference spectrum of $[\mathbf{Ru(bpy)_3}]^{+}$ and $[\mathbf{Ru(bpy)_3}]^{2+}$.

As replacements for $[\mathbf{Ru(bpy)_3}]^{2+}$, we also tested the complexes ruthenium-tris(phenanthroline) ($[\mathbf{Ru(phen)_3}]^{2+}$) and ruthenium-tris(4,7-diphenyl-1,10-phenanthroline) ($[\mathbf{Ru(dpp)_3}]^{2+}$). The excited states of these three light-harvesting compounds have very similar energies[S26] but widely differing lifetimes (670 ns, 1500 ns, and 6200 ns under our experimental conditions).

The expectation that a longer excited-state life increases the efficiency of reaction EnT is fulfilled with $[\mathbf{Ru(phen)_3}]^{2+}$, as the doubling of the $\mathbf{Py^{\bullet 2-}}$ concentration in Figure S8a demonstrates, but not with $[\mathbf{Ru(dpp)_3}]^{2+}$, where the maximum $\mathbf{Py^{\bullet 2-}}$ concentration is reached much later and is slightly lower than with $[\mathbf{Ru(bpy)_3}]^{2+}$. Because the emission spectra, *i.e.*, the triplet energies, of $^3[\mathbf{Ru(bpy)_3}]^{2+}$ and $^3[\mathbf{Ru(dpp)_3}]^{2+}$ are virtually identical also in our micellar environment (see, Figure S8b), the difference in the energy-transfer rate constants cannot be due to different energetics but can only be explained by a restricted access of the acceptor $\mathbf{Py^{-}}$ to the more lipophilic, hence more deeply embedded, donor $^3[\mathbf{Ru(dpp)_3}]^{2+}$.

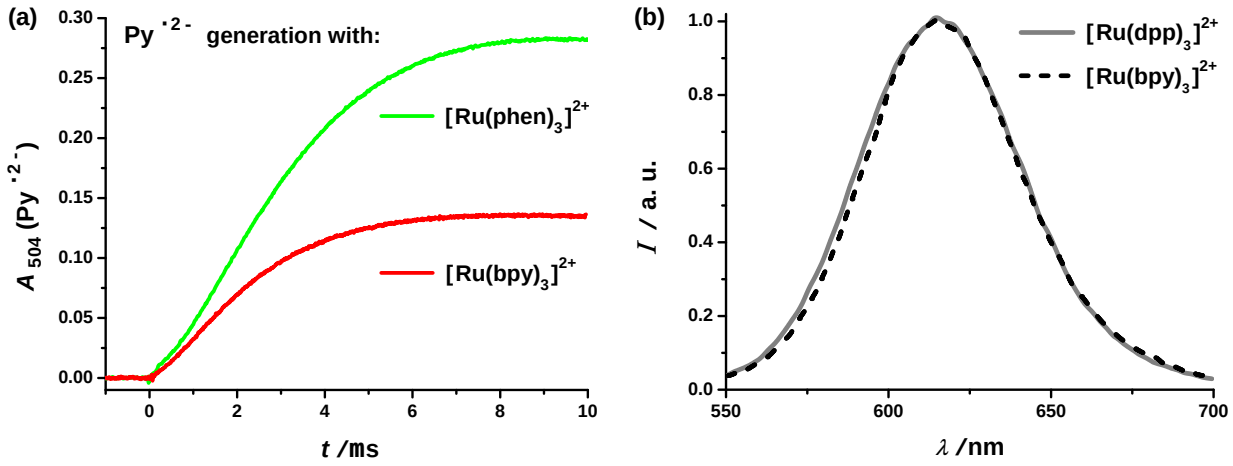

Figure S8: (a) Comparison of $\mathbf{Py^{\bullet 2-}}$ generation with the green-light excited complexes $[\mathbf{Ru(bpy)_3}]^{2+}$ and $[\mathbf{Ru(phen)_3}]^{2+}$ as sensitizers under the experimental conditions of Figure 2b (main paper). The laser intensities were adjusted such as to ensure identical concentrations of the excited donor in both experiments. (b) Normalized luminescence spectra of $[\mathbf{Ru(bpy)_3}]^{2+}$ and $[\mathbf{Ru(dpp)_3}]^{2+}$ in aqueous SDS (30 mM) solution at pH 12.7. For further explanation, see text.

3.6 Hydrated electron $\mathbf{e_{aq}^{\bullet -}}$

The absorption spectrum of $\mathbf{e_{aq}^{\bullet -}}$ was obtained by 308 nm photoionization of $\mathbf{Asc^{2-}}$ and subsequent spectral separation of the reaction products $\mathbf{Asc^{\bullet -}}$ and $\mathbf{e_{aq}^{\bullet -}}$, as described previously.[S24] For its calibration, the generally accepted molar absorption coefficient at maximum ($\varepsilon(\mathbf{e_{aq}^{\bullet -}}) = 22700\,M^{-1}\,cm^{-1}$)[S21] was used. Both the absorption spectrum and the natural life of $\mathbf{e_{aq}^{\bullet -}}$, 2.6 µs, are unaffected by the addition of SDS (30 mM) to our strongly alkaline solutions (pH 12.7).

In all photoionization experiments on $\mathbf{Py^{\bullet 2-}}$ (Sections 3.3 and 4 of the ESI, and Figure 3 of the main paper), we monitored $\mathbf{e_{aq}^{\bullet -}}$ at 824 nm ($\varepsilon_{824}(\mathbf{e_{aq}^{\bullet -}}) = 16900\,M^{-1}\,cm^{-1}$) because of an improved detection sensitivity at that wavelength[S1]. To separate the signals of $\mathbf{e_{aq}^{\bullet -}}$ from those of other absorbing species, we saturated the solutions with N_2O, which selectively removes $\mathbf{e_{aq}^{\bullet -}}$ within the duration of our laser pulses[S27] (compare, Figure S9b). The resulting hydroxyl radicals predominantly terminate by the reaction with the radical scavenger ascorbate[S28,S29], which is present in large excess compared to any other oxidizable substance in our system. In control experiments, where we omitted N_2O and instead separated the transients through parallel detection at several wavelengths, we did not observe any differences with respect to $\mathbf{Py^{\bullet 2-}}$ formation or bleaching.

In the absence of additives such as $\mathbf{ClCH_2COO^-}$, the main deactivation pathway (more than 96 %) of $\mathbf{e_{aq}^{\bullet -}}$ in the reaction system of the main paper (3×10^{-4} M $\mathbf{Py^-}$, 6×10^{-5} M $[\mathbf{Ru(bpy)_3}]^{2+}$, 1.5 mM $\mathbf{Asc^{2-}}$, 30 mM SDS) is its reaction with surplus redox catalyst $\mathbf{Py^-}$ (reaction S2). The rate constant of this reaction has been determined to be $1.5 \times 10^{10}\,M^{-1}\,s^{-1}$[S20] at pH 12.7 and, as we found, is practically identical in our reaction medium. Under our general conditions, the

scavenging of $\mathbf{e_{aq}^{\bullet-}}$ by $[\mathbf{Ru(bpy)_3}]^{2+}$, reaction S1, is a minor process ($2.7 \times 10^9\,M^{-1}\,s^{-1}$)[S30], which amounts to about 4 %.

To compare our rate constant for the decomposition of $\mathbf{ClCH_2COO^-}$ by $\mathbf{e_{aq}^{\bullet-}}$ (reaction (X), see Figure 3b of the main paper) with the literature, we extrapolated it with the Brønsted–Bjerrum equation[S29] to zero ionic strength. The result of that procedure, $0.82 \times 10^9\,M^{-1}\,s^{-1}$, is slightly lower than the recommended value, $1.0 \times 10^9\,M^{-1}\,s^{-1}$ [S29]. We trace this small derivation back to an overestimation of the correction for the kinetic salt effect, which frequently occurs at higher ionic strengths ($> 0.01\,M$)[S31].

4 Analyzing the green-light photoionization

4.1 $\mathbf{Py^{\bullet 2-}}$ bleaching

At the absorption maximum of $\mathbf{Py^{\bullet 2-}}$, 504 nm, the huge molar absorption coefficient of $60400\,M^{-1}\,cm^{-1}$ allows a sensitive detection and minimizes the contributions of all other absorbing transients (compare, Figure S4). In addition, the quasi-instantaneous contributions largely balance: The conversion of $[\mathbf{Ru(bpy)_3}]^{2+}$ into $^3[\mathbf{Ru(bpy)_3}]^{2+}$ by a laser pulse is accompanied by a negative absorption, which is slight because of the nearby isosbestic point at 514 nm and is almost completely compensated by the small amount of static energy transfer (see, Section 3.2) that turns $^3[\mathbf{Ru(bpy)_3}]^{2+}$ into the more strongly absorbing $^3\mathbf{Py^-}$. The remaining minute effects, as well as those of all slower processes, most notably the secondary formation of $\mathbf{Py^{\bullet 2-}}$ by the bleaching laser pulse, are all proportional to the amount of $^3[\mathbf{Ru(bpy)_3}]^{2+}$ produced by that pulse. Because the prepulse concentration of the redox catalyst differs from its weight-in concentration by less than 2%, the bleaching can be isolated simply by scaling the interpulse trace with a factor and subtracting it from the trace after the second pulse; the scaling factor is determined from the luminescence intensities (maximum, 620 nm) after each pulse, which are proportional to the $^3[\mathbf{Ru(bpy)_3}]^{2+}$ concentration but insensitive to all other species.

An example of that correction is displayed in Figure S9a. A comparison of the bleaching results in this complex system with those obtained in the simplified system (without $[\mathbf{Ru(bpy)_3}]^{2+}$; see Figure S7b) shows the validity of the described experimental procedure.

4.2 $\mathbf{e_{aq}^{\bullet-}}$ formation

At our detection wavelength for $\mathbf{e_{aq}^{\bullet-}}$, 824 nm (compare, Section 3.6), $^3[\mathbf{Ru(bpy)_3}]^{2+}$ [S32] and $\mathbf{Py^{\bullet 2-}}$ [S20] absorb as well, albeit slightly. To separate the signals, we carried out experiments with and without the selective $\mathbf{e_{aq}^{\bullet-}}$ scavenger N_2O[S27]. Their difference yields a zero line before the second ionizing laser flash (see, the violet trace displayed in Figure S9b) indicating the inertness of N_2O towards both the chemicals of our catalytic system and the exited states or radical species

present upon irradiation. However, after the second laser pulse, these measurements give a substantial difference, which is due to $\mathbf{e}_{aq}^{\bullet-}$. Whereas the initial rise of that difference signal only captures the $\mathbf{e}_{aq}^{\bullet-}$ formation, the subsequent decay to a nonzero offset is caused by reaction S2, which converts $\mathbf{e}_{aq}^{\bullet-}$ into absorbing $\mathbf{Py}^{\bullet 2-}$ (compare, Section 3.6) but occurs in the N_2O-free solution only.

In the presence of $\mathbf{ClCH_2COO^-}$, a further $\mathbf{e}_{aq}^{\bullet-}$ acceptor whose scavenging product does not absorb at 824 nm, the initial $\mathbf{e}_{aq}^{\bullet-}$ signal observed by the difference measurements remains constant but the offset decreases accordingly; this is in line with the competing scavenging of $\mathbf{e}_{aq}^{\bullet-}$ by $\mathbf{Py}^-$ and $\mathbf{ClCH_2COO^-}$. This offset does not adversely affect the determination of the $\mathbf{e}_{aq}^{\bullet-}$ lifetime by a monoexponential fit, as seen in the inset of Figure S9b.

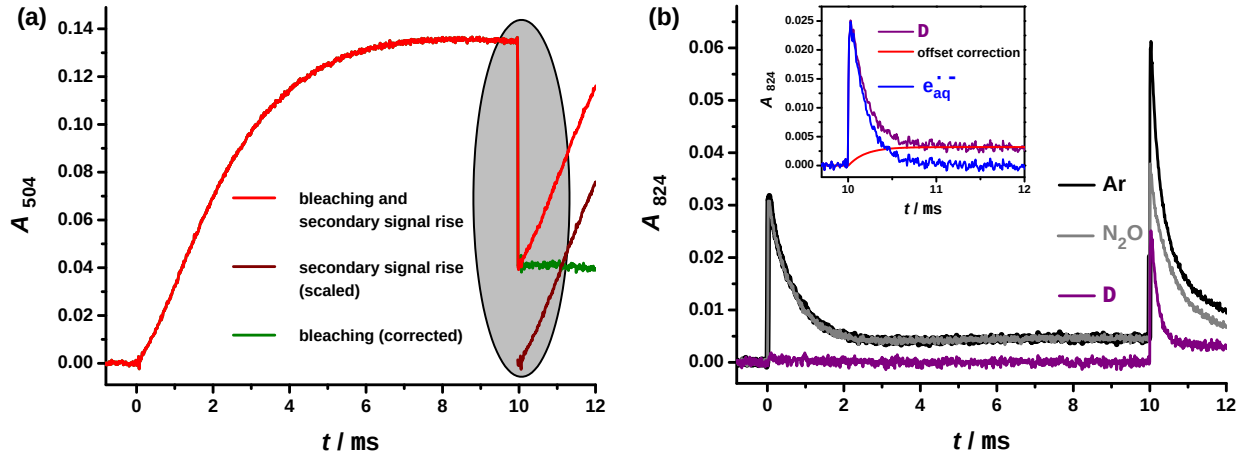

Figure S9: Extraction of the pure $\mathbf{Py}^{\bullet 2-}$ bleaching from the 504 nm trace (a) and separation of the $\mathbf{e}_{aq}^{\bullet-}$ signals from those of $\mathbf{Py}^{\bullet 2-}$ and $^3[\mathbf{Ru(bpy)_3}]^{2+}$ at 824 nm (b) in a green-light two-pulse laser flash photolysis measurement. Experimental conditions and pulse energies as in Figure 3a of the main paper. (a) To facilitate the $\mathbf{Py}^{\bullet 2-}$ bleaching analysis, which was carried out in N_2O-saturated solution to suppress $\mathbf{e}_{aq}^{\bullet-}$ signals, the $\mathbf{Py}^{\bullet 2-}$ formation and other reactions caused by the second pulse (red trace) are blanked by subtracting the interpulse trace (dark red trace), after multiplication with a weighting factor, from the trace following the second pulse. The weighting factor (1.08) takes into account the relative excitation of our energy donor by the two pulses and is given by the ratio of postpulse luminescences at 620 nm (which are directly proportional to the $^3[\mathbf{Ru(bpy)_3}]^{2+}$ concentrations). (b) The difference of the absorption traces in Ar-saturated (black) and N_2O-saturated solution nearly perfectly isolates the $\mathbf{e}_{aq}^{\bullet-}$ signal (violet). The only reaction that is not blanked by this procedure is the scavenging of $\mathbf{e}_{aq}^{\bullet-}$ by $\mathbf{Py}^-$ to give $\mathbf{Py}^{\bullet 2-}$, which absorbs at 824 nm and causes an offset in the violet curve (main plot). That further signal rise does not influence the initial $\mathbf{e}_{aq}^{\bullet-}$ signal and can be completely removed by a monoexponential fit with the $\mathbf{e}_{aq}^{\bullet-}$ lifetime and the observed offset as limit (inset). For further explanation, see text.

As we recently reported, the green-light photoionization of $[\mathbf{Ru(bpy)_3}]^{+}$ also yields $\mathbf{e_{aq}^{\bullet -}}$ [S1], so the small amount of $[\mathbf{Ru(bpy)_3}]^{+}$ formed through reaction Q during the interpulse delay can contribute to the overall accessible $\mathbf{e_{aq}^{\bullet -}}$ concentration as well. In consequence, the electron yield slightly surpasses the $\mathbf{Py^{\bullet 2-}}$ bleaching (Figure S9b). This contribution can be quantitatively determined by repeating the experiment under the same conditions but without $\mathbf{Py^{-}}$ (an example is given in Figure S10), and then eliminated by subtraction of the traces. This correction method has been applied to all measurements of the $\mathbf{e_{aq}^{\bullet -}}$ concentration in the main paper (Figure 3) and in the supplementary information (Figure S9b).

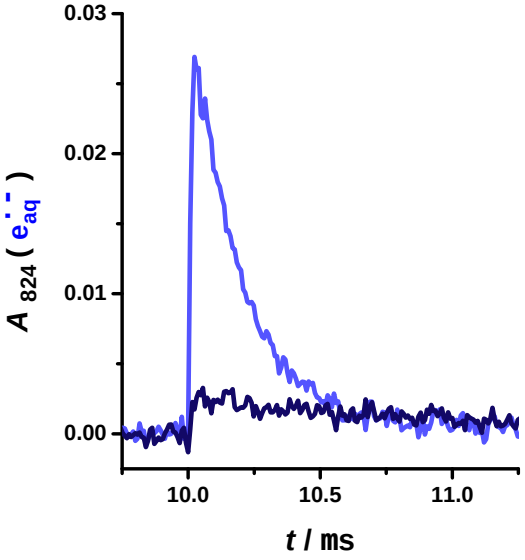

Figure S10: Identifying the contribution of $[\mathbf{Ru(bpy)_3}]^{+}$ photoionization to the $\mathbf{e_{aq}^{\bullet -}}$ signal at 824 nm by measurements with $\mathbf{Py^{-}}$ (light blue trace) and without $\mathbf{Py^{-}}$ (dark blue trace) under the conditions of Figure 3a (main paper).

5 Supplementary references

[S1] M. Goez, C. Kerzig, R. Naumann, *Angew. Chem. Int. Ed.* **2014**, *53*, 9914–9916.

[S2] M. B. Davies, J. Austin, D. A. Partridge, *Vitamin C: Its Chemistry and Biochemistry*, The Royal Society of Chemistry, Cambridge, 1st edn, **1991**.

[S3] M. J. Frisch, G. W. Trucks, H. B. Schlegel, G. E. Scuseria, M. A. Robb, J. R. Cheeseman, G. Scalmani, V. Barone, B. Mennucci, G. A. Petersson, H. Nakatsuji, M. Caricato, X. Li, H. P. Hratchian, A. F. Izmaylov, J. Bloino, G. Zheng, J. L. Sonnenberg, M. Hada, M. Ehara, K. Toyota, R. Fukuda, J. Hasegawa, M. Ishida, T. Nakajima, Y. Honda, O. Kitao, H. Nakai, T. Vreven, J. A. Montgomery, Jr., J. E. Peralta, F. Ogliaro, M. Bearpark, J. J. Heyd, E. Brothers, K. N. Kudin, V. N. Staroverov, R. Kobayashi, J. Normand, K. Raghavachari, A. Rendell, J. C. Burant, S. S. Iyengar, J. Tomasi, M. Cossi, N. Rega, J. M. Millam, M. Klene, J. E. Knox, J. B. Cross, V. Bakken, C. Adamo, J. Jaramillo, R. Gomperts, R. E. Stratmann, O. Yazyev, A. J. Austin, R. Cammi, C. Pomelli, J. W. Ochterski, R. L. Martin, K. Morokuma, V. G. Zakrzewski, G. A. Voth, P. Salvador, J. J. Dannenberg, S. Dapprich, A. D. Daniels, Ö. Farkas, J. B. Foresman, J. V. Ortiz, J. Cioslowski, D. J. Fox, *Gaussian 09 Revision B.01*, Gaussian Inc., Wallingford CT, 2009.

[S4] N. V. Nucci, B. Zelent, J. M. Vanderkooi, *J. Fluoresc.* **2008**, *18*, 41–49.

[S5] A. Adhikary, A. Kumar, D. Becker, M. D. Sevilla, *J. Phys. Chem. B* **2006**, *110*, 24171–24180.

[S6] M. C. Foti, C. Daquino, I. D. Mackie, G. A. DiLabio, K. U. Ingold, *J. Org. Chem.* **2008**, *73*, 9270-–9282.

[S7] M. Goez, C. Kerzig, *Angew. Chem. Int. Ed.* **2012**, *51*, 12606–12608.

[S8] C. J. Cramer, *Essentials of Computational Chemistry: Theories and Models*, Wiley, Chichester, 2nd edn, **2004**.

[S9] B. Zelent, J. M. Vanderkooi, N. V. Nucci, I. Gryczynski, Z. Gryczynski, *J. Fluoresc.* **2009**, *19*, 21–31.

[S10] E. V. Donckt, R. Dramaix, J. Nasielski, C. Vogels, *Trans. Faraday Soc.* **1969**, *65*, 3258–3262.

[S11] M. Montalti, A. Credi, L. Prodi, M. T. Gandolfi, *Handbook of Photochemistry*, Taylor and Francis, Boca Raton, 3rd edn, **2006**.

[S12] H. A. Benesi, J. H. Hildebrand, *J. Am. Chem. Soc.* **1949**, *71*, 2703–2707.

[S13] N. J. Turro, M. Grätzel, A. M. Braun, *Angew. Chem. Int. Ed.* **1980**, *19*, 675–696.

[S14] F. H. Quina, V. G. Toscano, *J. Phys. Chem.* **1977**, *81*, 1750–1754.

[S15] C. Bohne, E. B. Abuin, J. C. Scaiano, *J. Am. Chem. Soc.* **1990**, *112*, 4226–4231.

[S16] Y. Mori, H. Shinoda, T. Nakano, T. Kitagawa, *J. Phys. Chem. A* **2002**, *106*, 11743–11749.

[S17] J. R. Lakowicz, *Principles of Fluorescence Spectroscopy*, Springer, New York, 3rd edn, **2010**.

[S18] U. Lachish, M. Ottolenghi, J. Rabani, *J. Am. Chem. Soc.* **1977**, *99*, 8062–8063.

[S19] A. M. Funston, S. V. Lymar, B. Saunders-Price, G. Czapski, J. R. Miller, *J. Phys. Chem. B* **2007**, 6895–6902.

[S20] Y. Yamamoto, *J. Chem. Soc., Perkin Trans. 2* **1994**, 1555–1559.

[S21] P. M. Hare, E. A. Price, D. M. Bartels, *J. Phys. Chem. A* **2008**, *112*, 6800–6802.

[S22] C. Kerzig, M. Goez, *Phys. Chem. Chem. Phys.* **2014**, *16*, 25342–25349.

[S23] P. Wardman, *J. Phys. Chem. Ref. Data* **1989**, *18*, 1637–1755.

[S24] C. Kerzig, M. Goez, *Phys. Chem. Chem. Phys.* **2015**, *17*, 13829–13836.

[S25] B. H. J. Bielski, H. W. Richter, *Ann. N. Y. Acad. Sci.* **1975**, *258*, 231–237.

[S26] A. A. Vlcek, E. S. Dodsworth, W. J. Pietro, A. B. P. Lever, *Inorg. Chem.* **1995**, *34*, 1906–1913.

[S27] J. W. T. Spinks, R. J. Woods, *An Introduction to Radiation Chemistry*, Wiley, New York, 2nd edn, **1976**.

[S28] J. I. Mujika, J. M. Matxain, *J. Mol. Model.* **2013**, *19*, 1945–1952.

[S29] G. V. Buxton, C. L. Greenstock, W. P. Helman, A. B. Ross, *J. Phys. Chem. Ref. Data* **1988**, *17*, 513–886.

[S30] D. Meisel, M. S. Matheson, J. Rabani, *J. Am. Chem. Soc.* **1978**, *100*, 117–122.

[S31] A. A. Frost, R. G. Pearson, *Kinetics and Mechanism*, John Wiley and Sons, New York, 2nd edn, **1961**.

[S32] O. Shimizu, J. Watanabe, S. Naito, *Chem. Phys. Lett.* **2000**, *332*, 295–298.